CHEMISTRY OF MATERIALS

pubs.acs.org/cm

Article

Exploration of Oxyfluoride Frameworks as Na-ion Cathodes

Published as part of Chemistry of Materials special issue "Celebrating the 25th Anniversary of the Chemical Research Society of India".

Debolina Deb and Gopalakrishnan Sai Gautam*

Cite This: *Chem. Mater.* 2024, 36, 11892−11904

Read Online

ACCESS | Metrics & More | Article Recommendations | Supporting Information

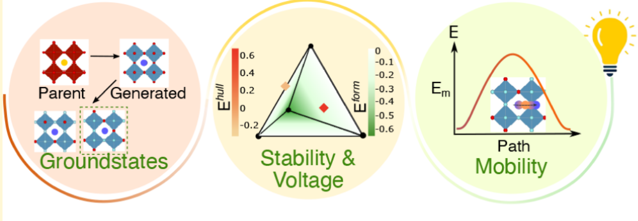

Roadmap to find potential oxyfluorides as Na-ion battery cathode

ABSTRACT: Na-ion batteries (NIBs) are increasingly considered as a viable alternative to Li-ion batteries due to the abundance, low cost, and thermal stability of Na-based systems. To improve the practical utilization of NIBs in applications, it is important to boost the energy and power densities of the electrodes being used by the discovery of novel candidate materials. Thus, we explore the chemical space of transition metal-containing oxyfluorides (TMOFs) that adopt a perovskite structure as possible NIB electrodes. Our choice of the perovskite structure is motivated by the "large" cationic tunnels that can accommodate Na^+, while the chemistry of TMOFs is motivated by the high electronegativity and inductive effect of F^-, which can possibly lead to higher voltages. We use density functional theory-based calculations to estimate the ground state polymorphs, average Na (de)intercalation voltages, thermodynamic stabilities, and Na^+ mobility on two distinct sets of compositions: the F-rich Na_xMOF_2 and the O-rich $Na_{1+x}MO_2F$, where $x = 0-1$ and M = Ti, V, Cr, Mn, Fe, Co, or Ni. Upon identifying the ground state polymorphs in the charged compositions (i.e., MOF_2 and $NaMO_2F$), we show that F-rich perovskites exhibit higher average voltages compared to those of the O-rich perovskites. Also, we find six stable/metastable perovskites in the F-rich space, while all the O-rich perovskites (except $NaTiO_2F$) are unstable. Finally, our Na-ion mobility calculations indicate that $TiOF_2-NaTiOF_2$, $VOF_2-NaVOF_2$, $CrOF_2$, and $NaMnOF_2$ can be promising compositions, albeit with challenges to be resolved, for experimental exploration as NIB cathodes. These oxyfluoride compositions can be promising if used primarily in a strained electrode configuration and/or in thin film batteries. Our computational approach and findings provide insights into developing practical NIBs involving fluorine-containing intercalation frameworks.

■ INTRODUCTION

Na-ion battery (NIB) technology is a key contributor in reducing the extensive dependence on Li-ion batteries (LIBs) to fulfill the ever-increasing energy demands.[1−5] As a technology, NIBs have come a long way with notable applications in both electric vehicles and stationary energy storage.[6−9] Nevertheless, the practical utility of NIBs can be further enhanced with the development of novel high energy and power density electrode materials. While layered transition-metal oxides (TMOs) are the state-of-the-art NIB positive electrodes (cathodes),[10] the structural instabilities of layered compounds at their fully desodiated states and detrimental phase transitions have directed research toward polyanionic cathode frameworks.[11−13] Some of the most explored polyanionic frameworks, such as sodium superionic conductors (NaSICONs), alluaudites, olivines, and pyro/fluoro-phosphates, display a wide range of electrochemical performance and good structural stability, with low gravimetric capacity being a common impediment.[12] Thus, an ideal NIB cathode must be able to (de)intercalate the large Na^+ at high rates, without compromising structural stability, and deliver a large capacity for achieving both high energy and power densities. An ideal NIB negative electrode (anode) also has similar requirements as the ideal cathode.

Oxide perovskites, which have a general formula of ABO_3, where A and B are cations, have been explored for several applications beyond energy-storage, due to their structural stability and compositional flexibility.[14−18] Importantly, perovskites are suitable structures for accommodating Na^+ because of their rigid open structures with large voids.[19] Additionally, the incorporation of fluorides in cathode frameworks often leads to improved energy densities, since the higher electronegativity of F^- typically leads to a higher (de)intercalation voltage via the induction effect.[20−22] Indeed, many of the best-performing polyanionic NIB cathodes contain fluorine.[23−25]

Received: August 23, 2024
Revised: November 28, 2024
Accepted: December 2, 2024
Published: December 12, 2024

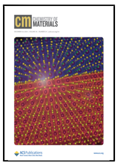

https://doi.org/10.1021/acs.chemmater.4c02374

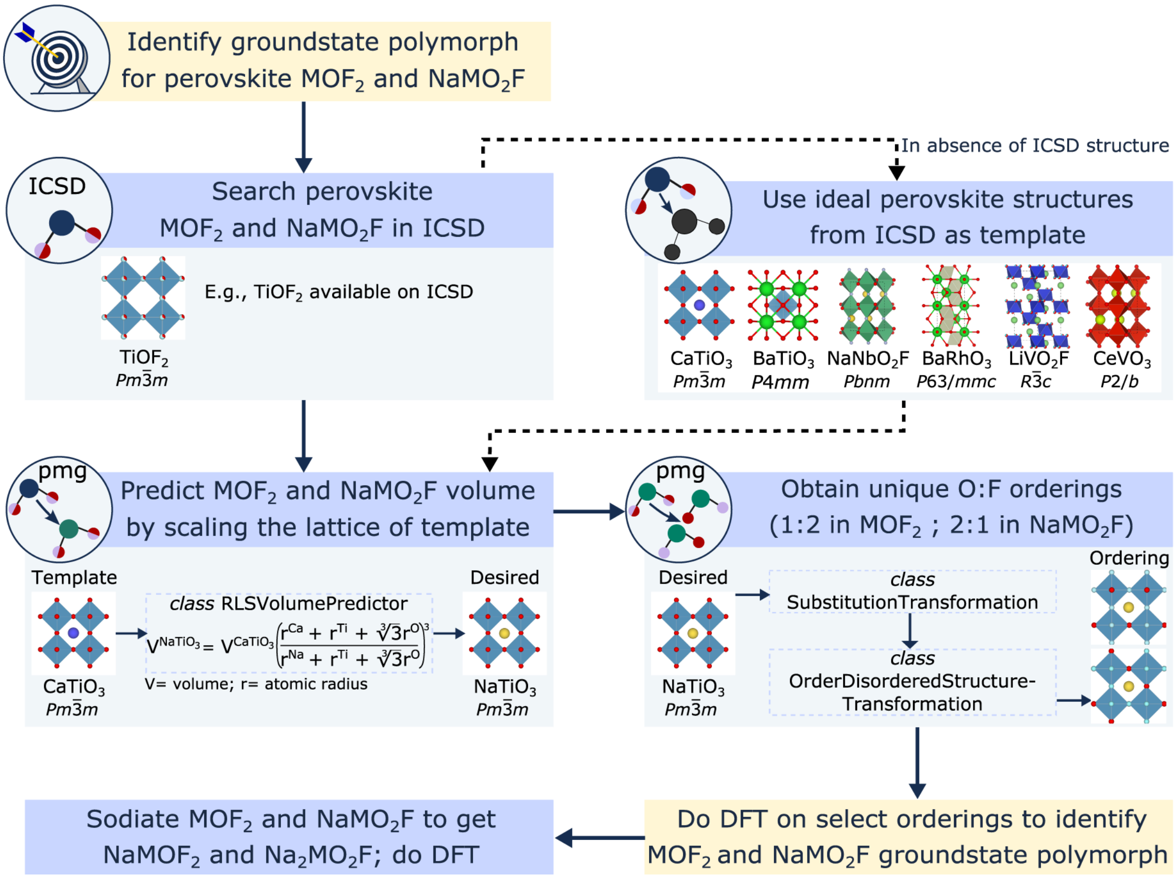

Figure 1. Workflow to obtain the ground state polymorph for desodiated F-rich MOF_2 and O-rich $NaMO_2F$ perovskites, where M = Ti, V, Cr, Mn, Fe, Co, or Ni. Notations "pmg" and "ICSD" refer to the pymatgen package and the inorganic crystal structure database.

Thus, fixing the A cation in a perovskite as Na^+, the B cation to be a redox-active 3*d* transition metal (TM), and the anions being a mixture of both O and F yields a class of perovskite-based TM oxyfluoride (TMOF) compositions as potential NIB cathodes (or anodes).

So far, perovskite TMOFs are a largely unexplored class of battery cathodes (or anodes), primarily due to synthesis difficulties from highly stable fluoride precursors.[26] Indeed, only a few TMOFs, including, $TiOF_2$ (space group: $Pm\bar{3}m$),[27] VO_2F ($R\bar{3}c$),[28,29] and NbO_2F ($Pm\bar{3}m$),[27] have been investigated as LIB cathodes. Additionally, Li_2MO_2F with M across the 3*d* series[30] and Na_2MnO_2F[31] have been reported to exhibit a disordered rocksalt and not a perovskite-based structure. Also, most of the oxyfluoride structures that have been reported have undergone either amorphization or an irreversible structural transition during electrochemical cycling.[32−35] Although Li-ion mobility is not hindered in both disordered rocksalt[36] and amorphized[37] oxyfluorides, studies have not analyzed Na-ion mobility in similar frameworks. Notably, the rutile-FeOF ($P4_2/mnm$) structure was tested as a NIB cathode and showed a reversible transition to cubic-Na_xFeOF.[35] However, this FeOF↔Na_xFeOF transition was accompanied by significant hysteresis in the corresponding voltage−capacity profiles, with possible contributions from electrolyte decomposition and/or other side reactions.[35] Importantly, the chemical class of TMOFs has not been systematically explored, either computationally or experimentally, as NIB cathodes, so far.

Here, we present a systematic density functional theory (DFT)-based computational exploration of perovskite-based TMOF compositions as potential NIB cathodes (or anodes). Specifically, we explore the chemical compositions of oxygen-rich ($NaMO_2F$ ↔ Na_2MO_2F) and fluorine-rich (MOF_2 ↔ $NaMOF_2$) perovskites, where M = Ti, V, Cr, Mn, Fe, Co, or Ni. For both the O-rich and F-rich compositions, we examine possible crystalline structures of the general perovskite framework. Importantly, we have evaluated the ground state Na-vacancy configurations, average Na intercalation voltages, and 0 K thermodynamic stabilities in both O-rich and F-rich TMOFs, followed by an evaluation of the Na-ion mobility in a subset of candidate compounds. Besides shedding light on the overall trends in voltages and stabilities, we also identify a few promising compositions, namely, $TiOF_2$−$NaTiOF_2$, VOF_2−$NaVOF_2$, $CrOF_2$, and $NaMnOF_2$, as candidate NIB electrodes, which can be relevant for subsequent experimental validation, primarily in strained configurations. We hope that our study opens up the novel oxyfluoride chemical space for battery cathode applications and beyond.

■ METHODS AND WORKFLOW

Structure Identification. To explore the TMOF chemical space, we used the charged-O (i.e., $NaMO_2F$) and F-rich (MOF_2) compositions as the initial cases of the structure generation for all TMs. Note that both charged compositions correspond to the TM being in a +4 oxidation state, while the corresponding discharged compositions (Na_2MO_2F and $NaMOF_2$) reflect the TM in a +3 oxidation state. To identify

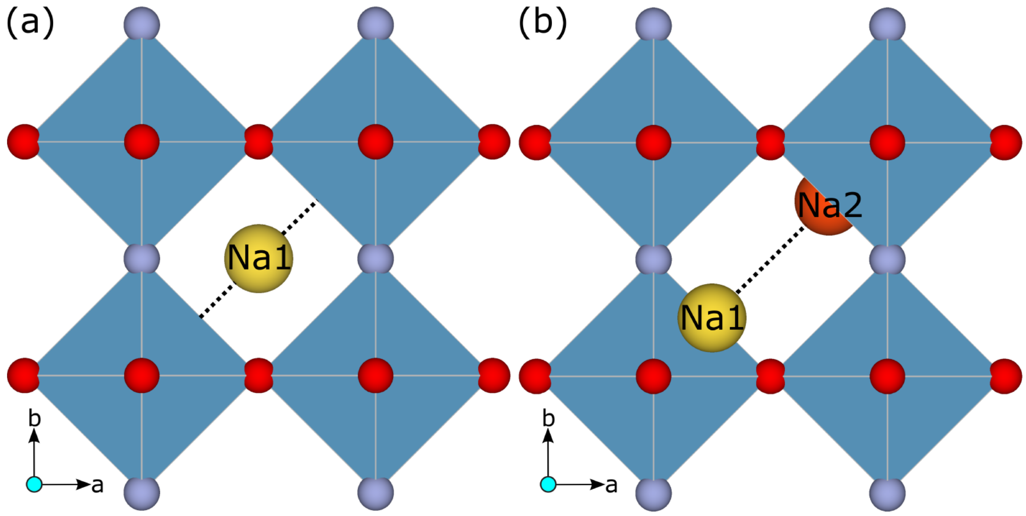

Figure 2. (a) $NaTiO_2F$ with the initial Na atom (denoted by Na1) at the center of the cube (i.e., fractional coordinates of (0.5, 0.5, 0.5)). (b) Displacement of the Na1 atom to (0.25, 0.25, 0.25) and the subsequent occupation of the second Na atom (denoted by Na2) at (0.75, 0.75, 0.75). Blue polyhedra in both panels denote TiO_4F_2 octahedra. O and F are represented by red and purple spheres, respectively. Body diagonals within the cubic structures are indicated by dotted black lines.

the relevant space group/polymorph, we first searched the inorganic crystal structure database (ICSD)[38] for experimental structures with the $NaMO_2F$ and MOF_2 compositions, where we found only $TiOF_2$ (ICSD collection code 160661; $Pm\bar{3}m$), VO_2F (ICSD collection code 142594; $R\bar{3}c$), and $LiVO_2F$ (ICSD collection code 142596; $R\bar{3}c$). Thus, we used the $TiOF_2$ structure from the ICSD as the starting configuration for all calculations involving cubic-$TiOF_2$, VO_2F for calculations of rhombohedral-MOF_2, and $LiVO_2F$ for calculations of rhombohedral-$NaMO_2F$.

Given the absence of ICSD structures for other TMOFs, we theoretically generated possible structures for both charged compositions using the workflow displayed in Figure 1. Similar to the procedure used in a previous study,[18] we used experimental template structures among six different space groups that are commonly adopted by perovskite compositions to generate six possible theoretical structures for each composition. Specifically, we used $CaTiO_3$, $BaTiO_3$, $NaNbO_2F$, $BaRhO_3$, $LiVO_2F$, and $CeVO_3$ as templates for the $Pm\bar{3}m$, $P4mm$, $Pbnm$, $P63/mmc$, $R\bar{3}c$, and $P2/b$ space groups, respectively. Note that we did not consider any ReO_3-type[19] (or perovskite-type) hydroxides, Prussian blue analogs, or formate compositions as templates largely due to the presence of water molecules and/or incompatibilities in the size of A-cation required in such structures.

We chose Ba and Ca containing structures as templates due to the similarity in the ionic radii of Ba^{2+} and Ca^{2+} to Na^+. Although $CaTiO_3$ is known to be an orthorhombic perovskite,[39] we used $CaTiO_3$ as a template for the cubic perovskite owing to the similarity in the ionic radii of Na^+ and Ca^{2+}[40] and the availability of the Ca-containing perovskite structure[41] in the ICSD. $CeVO_3$ was the only reasonable monoclinically distorted perovskite template we could find. For rhombohedral perovskites, the presence of VO_2F and $LiVO_2F$ experimental structures provided us both an oxyfluoride template along with possible Na sites, as Li can be substituted with Na,[42] motivating our use of $LiVO_2F$ as the template.[28] As far as the orthorhombic perovskite, $NaNbO_2F$ is an oxyfluoride and contains Na, and hence, it was the obvious choice as a template. Note that we used the $TiOF_2$ structure as the $Pm\bar{3}m$ template for $NaMO_2F$ compositions. In addition, we used the VO_2F structure as the $R\bar{3}c$ template for all rhombohedral-MOF_2 compositions and the $LiVO_2F$ structure as the $R\bar{3}c$ template for all rhombohedral-$NaMO_2F$ compositions.

From each template structure, we performed chemical substitution (i.e., replace Ca/Ba/Li/Ce with Na and the remaining cation with a 3*d* TM), to result in a $NaMO_3$ composition. Subsequenty, we used the RLSVolumePredictor[43] class of the pymatgen package to scale the lattice parameters of the template structure to values that better represent a $NaMO_3$ perovskite composition. Upon lattice scaling, we introduced F, based on an O:F ratio of 2:1 in O-rich perovskites and 1:2 in F-rich perovskites, by inducing disorder within the anionic sublattice using the SubstitutionTransformation class of pymatgen. Note that in F-rich perovskites, we removed Na before the lattice scaling step. Finally, we enumerated symmetrically distinct O−F arrangements for all distinct template space groups in both the $NaMO_2F$ and MOF_2 compositions, using the OrderDisorderedStructureTransformation class of pymatgen, and performed DFT calculations to determine the respective ground state configurations. During enumerations, we took a maximum of 16 structures that exhibited the lowest electrostatic energy, calculated using the Ewald summation technique,[44] to minimize computational expense. In the case of $P4mm$ and $R\bar{3}c$ perovskites (both MOF_2 and $NaMOF_2$), we obtained a total of only five and three symmetrically distinct configurations upon enumeration and all configurations were considered for DFT calculations. In the case of $Pm\bar{3}m$, $Pbnm$, $P63/mmc$, and $P2/b$ space groups, we obtained a total of 22, 40, 55, and 48 symmetrically distinct configurations, respectively, out of which we chose the 16 lowest electrostatic energy configurations for each space group (for both MOF_2 and $NaMOF_2$).

Once the ground state polymorph of each desodiated $NaMO_2F$ and MOF_2 composition was determined, we added Na to the DFT-relaxed charged ground state structures to obtain the corresponding discharged (or sodiated) configurations, i.e., Na_2MO_2F and $NaMOF_2$. For $NaMOF_2$, we initialized the Na ions on the sites occupied by the A-cation in the corresponding template perovskite structure. Given that the $NaMOF_2$ perovskite only has one distinct Na (or A cation) site, we created a second Na site by displacing the existing Na ion to minimize electrostatic repulsion between the two Na ions, as displayed in Figure 2. For example, in the case of $Pm\bar{3}m$ $NaTiO_2F$, we displaced the existing Na from the center of the cube (i.e., fractional coordinates of (0.5, 0.5, 0.5)) along the body diagonal to a new site of coordinates (0.25, 0.25, 0.25). Subsequently, we initialized the second Na atom at the coordinates of (0.75, 0.75, 0.75), to minimize electrostatic repulsions between the two Na. The introduction of additional Na sites in other perovskite structures is described in the Supporting Information, along with a schematic in Figure S1.

Computational Details. We used the Vienna ab initio simulation package (VASP)[45,46] for all spin-polarized DFT calculations. We utilized the projector augmented-wave (PAW)[47,48] potentials similar to our previous work,[49−51] with the list of PAW potentials used in this work compiled in Table S1. To account for the electronic exchange and correlation, we employed the Hubbard U corrected,[52,53] strongly constrained and appropriately normed (i.e., SCAN+U)[49,50,54] functional. We utilized U values that were obtained for TMOs in our work,[49,50] since they gave the best agreement between the calculated and experimental average voltages in Li-based TMOFs (see Table S2). We expanded the one-electron wave functions using a plane wave basis set, with a 520 eV kinetic energy cutoff, and used a Gaussian smearing of width 0.05 eV to integrate the Fermi surface. We sampled the irreducible Brillouin zone with a Γ-centered Monkhorst-pack[55] k-mesh with a density of at least 32 k-points per Å (i.e., a minimum sampling of 32 subdivisions along each unit reciprocal lattice vector). For the total energies and atomic forces, we set the convergence criterion to be 0.01 meV and $|0.03|$ eV/Å, respectively. To reduce computational complexity, we initialized all 3d TMs in their corresponding high-spin ferromagnetic configurations. For all structures, we relaxed the cell volume, cell shape, and ionic positions without preserving any symmetry. Where possible, we have followed a color-blind friendly color scheme in our plots.[56]

Tolerance Factors. We calculated the Goldschmidt tolerance factor (t)[57] using eq 1 for Na-TMOFs, which adhere to the ABO_3-type stoichiometry.[57] Compositions with corner-shared octahedra (i.e., $Pm\bar{3}m$, $P4mm$, $Pbnm$, and $P2/b$ space groups) and with $0.825 < t < 1.059$ are 74% likely to be accurately labeled as an ideal perovskite structure.[57,58] For compositions with isolated octahedra (i.e., $P63/mmc$, and $R\bar{3}c$), t should ideally label the structures as nonperovskites. In eq 1, r_A represents the Shannon ionic radii of 12-coordinated Na^+, while r_B signifies the Shannon radii of 6-coordinated TM^{3+} and TM^{4+} for sodiated and desodiated TMOF, respectively. r_X denotes the weighted Shannon radii of the of 6-coordinated anion, with the weights corresponding to the relative content of O and F in the TMOF.[59] For the Na_2MO_2F compositions, we used r_A of a single 12-coordinated Na^+ and r_B to be 6-coordinated TM^{3+} for the sake of comparison with other TMOF compositions considered, even though t is not actually developed for A_2BO_3 compositions. We also utilized eq 2 to calculate the tolerance factor (τ) developed by Bartel et al.,[60] which has a 92% accuracy rate in correctly labeling compositions with perovskite structures as a perovskite. τ takes into account the oxidation state of Na (denoted as n_A), apart from r_A, r_B, and r_X used for t, and considers a structure an ideal perovskite when $\tau < 4.18$.[60] Note that both t and τ factors cannot be applied to the MOF_2 stoichiometry due to the absence of the A-cation in the structure.

$$t = \frac{r_A + r_X}{\sqrt{2}(r_B + r_X)} \tag{1}$$

$$\tau = \frac{r_X}{r_B} - n_A\left(n_A - \frac{r_A/r_B}{\ln(r_A/r_B)}\right) \tag{2}$$

Ab Initio Thermodynamics. For evaluating the thermodynamic stability of the TMOFs considered, we constructed the 0 K convex hull of the corresponding quaternary (i.e., Na−TM−O−F) chemical spaces by using the pymatgen package. Specifically, we collected experimentally reported structures of individual elements (Na, TM, O, and F), binaries (Na−O, Na−F, TM−O, and TM−F), ternaries (Na−O−F, TM−O−F, Na−TM−O, Na−TM−F), and quaternaries (Na−TM−O−F) from the ICSD and subsequently calculated their total energies using DFT. Note that we only considered ICSD structures that were fully ordered; i.e., each lattice site in a structure exhibits an integer occupation of a given species. Also, for individual elements, Na−O and Na−F binaries, and Na−O−F ternaries, we used only the SCAN functional for treating the electronic exchange and correlation, while for the other structures, we used the SCAN+U functional. Since we have utilized only DFT-calculated total energies to construct the 0 K convex hull, our phase diagrams do not include the $p-V$ contributions.

Importantly, any stable entity on the 0 K convex hull will have a energy above convex hull (E^{hull}) as 0 meV/atom, while any metastable/unstable entity will have $E^{hull} > 0$.[61] Given that compounds that are metastable at 0 K can be stabilized under different experimental conditions, we used a synthesizeability threshold of $E^{hull} \leq 100$ meV/atom.[62] This implies that compounds with a $E^{hull} \leq 100$ meV/atom may be synthesized under higher temperatures/pressures and can be considered metastable, while compounds with $E^{hull} > 100$ meV/atom are unlikely to be synthesized and can be considered to be unstable. All calculated phase diagrams (except for the Na−Ti−O−F quaternary) are compiled in Figure S4, while the list of stable/unstable compounds is compiled in Table S5.

The average voltage for Na (de)intercalation in TMOFs is evaluated using DFT-based total energies from the well-known Nernst equation.[63] Considering a Na (de)intercalation reaction of the form, $Na_xTMOF + \Delta xNa \leftrightarrow Na_{x+\Delta^x}TMOF$, we can approximate the Gibbs energy change (ΔG) associated with the (de)intercalation process using eq 3, which neglects entropic and $p-V$ contributions. Note that the E terms in eq 3 are DFT-calculated, with Na_xTMOF and $Na_{x+\Delta x}TMOF$ described with SCAN+U and metallic Na described with SCAN in its body-centered-cubic ground state. F is Faraday's constant.

$$\langle V \rangle = -\frac{\Delta G}{\Delta xF} \approx -\frac{E(Na_{x+\Delta x}TMOF) - [E(Na_xTMOF) + \Delta xE(Na)]}{\Delta xF} \tag{3}$$

Kinetics. To estimate the ionic mobility of Na^+ in the selected TMOF frameworks, we utilized a DFT-based nudged elastic band (NEB)[64,65] calculations to estimate the migration barrier (E_m) associated with Na^+ motion. For all structures, we considered a vacancy-mediated Na^+ migration along the A-site "tunnel" of the perovskite framework and calculated E_m either

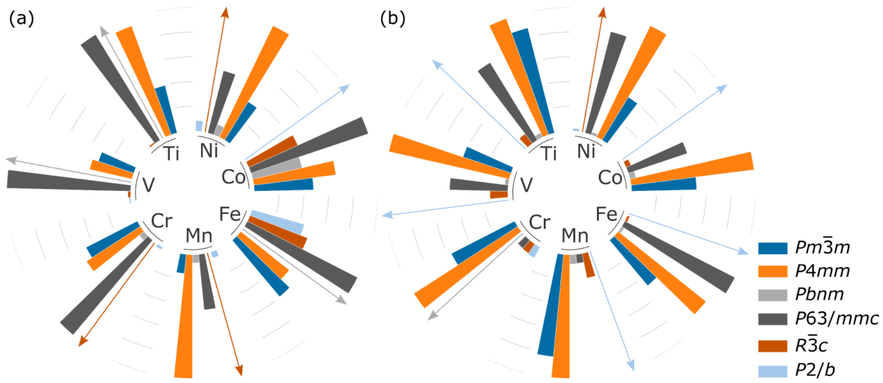

Figure 3. Percentage-normalized relative energies of all polymorphs considered with respect to the corresponding ground states for (a) F-rich MOF_2 and (b) O-rich $NaMO_2F$. All ground state polymorphs are indicated by colored solid arrows as per the color of the respective ground state polymorph. Each concentric ring on the radars represents a percentage step of 20%.

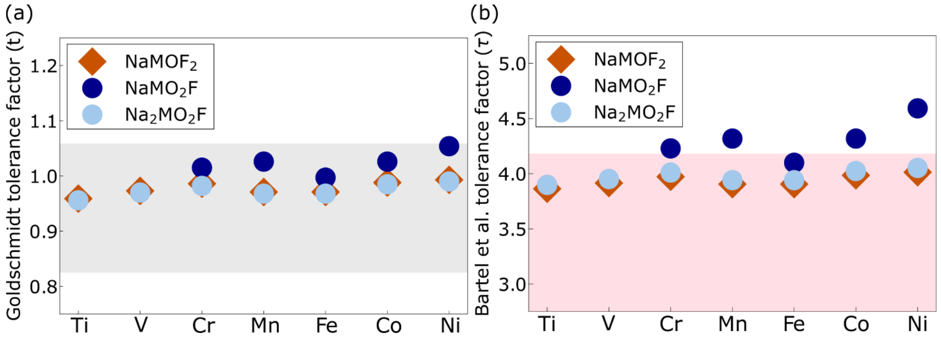

Figure 4. Calculated (a) Goldschmidt (t) and (b) Bartel et al. (τ) tolerance factors for $NaMOF_2$ (orange diamonds), $NaMO_2F$ (dark blue circles), and Na_2MO_2F (light blue circles). Threshold values for perovskite formation, namely $0.825 < t < 1.059$ and $\tau < 4.18$ are indicated by the shaded gray and shaded pink regions in panels a and b, respectively.

at the charged or the discharged sodium concentration limits. Upon introducing a Na-vacancy and fully relaxing the end point configurations, we interpolated five images across the end points to initialize the minimum energy path (MEP).

A spring constant of 5 eV/Å^2 was introduced between the images, and we considered the NEB calculation converged when the total energy of each image and the perpendicular component of the force between each image dropped below 0.01 meV and |0.05| eV/Å, respectively. For all NEB calculations, we used supercells with lattice parameters of ≥8 Å to avoid spurious interactions of the migrating Na with its periodic images. We used the Perdew−Burke−Ernzerhof (PBE)[66] parametrization of the generalized gradient approximation (GGA) to describe the exchange-correlation in our NEB calculations instead of SCAN, since GGA provides accurate qualitative trends at lower computational cost and with fewer convergence difficulties.[67] We performed full structure relaxations of our initial and final images with GGA before performing the NEB. All computed MEPs are compiled in Figure S5, and the Na^+ migration pathway in $TiOF_2$ is illustrated in Figure S6.

■ RESULTS

Ground State Polymorphs. The ground state polymorphs for each desodiated F-rich MOF_2 and O-rich $NaMO_2F$ are represented by the black arrows in panels *a* and *b* of Figure 3. The percentage normalized differences in energies of the other polymorphs considered, relative to the ground state, are plotted as bars in Figure 3. Specifically, we have plotted the percentage differences, calculated as $\frac{E(\text{polymorph}) - E(\text{ground state})}{E(\text{highest-energy polymorph}) - E(\text{ground state})} \times 100$, where each concentric ring on the radars represent percentage steps of 20%. Thus, the ground state and the highest energy polymorph represent 0% and 100%, respectively, on the radar of Figure 3 for each composition. Notably, the ground state polymorphs of the MOF_2 compositions include *Pbnm* (for Ti, V, Fe), $R\bar{3}c$ (Cr, Mn, Ni), and *P2/b* (Co), while those of the $NaMO_2F$ compositions are *P2/b* (Ti, V, Mn, Fe, Co), *Pbnm* (Cr), and $R\bar{3}c$ (Ni). We have compiled the percentage normalized relative energies and the actual relative energies for all perovskite polymorphs considered in Tables S3 and S4, respectively, and provided the schematics of the desodiated ground states and their corresponding sodiated structures in Figure S2.

Figure 4 displays the t and τ tolerance factors estimated for F-rich $NaMOF_2$ and for O-rich $NaMO_2F$ and Na_2MO_2F, with their respective values tabulated in Table S7. We have also compiled the t and τ values for Li-based perovskite TMOFs, with compositions of $LiMOF_2$, $LiMO_2F$, and Li_2MO_2F given in Table S7 for comparison.

Notably, all the Na-TMOF stoichiometries lie within the range of $0.825 < t < 1.059$,[57] as shown in Figure 4a, indicating that t could correctly label compositions with ground state polymorphs as *Pbnm* (F-rich $NaMOF_2$ with M as Ti, V, and Fe, and O-rich $NaMO_2F$ and Na_2MO_2F with M as Cr) and *P2/b* (F-rich $NaMOF_2$ with M as Co and O-rich $NaMO_2F$ and Na_2MO_2F with M as Ti, V, Mn, Fe, and Co) as perovskites. However, t of compositions with rhombohedral or hexagonal perovskite structures should lie outside the range of $0.825 < t <$

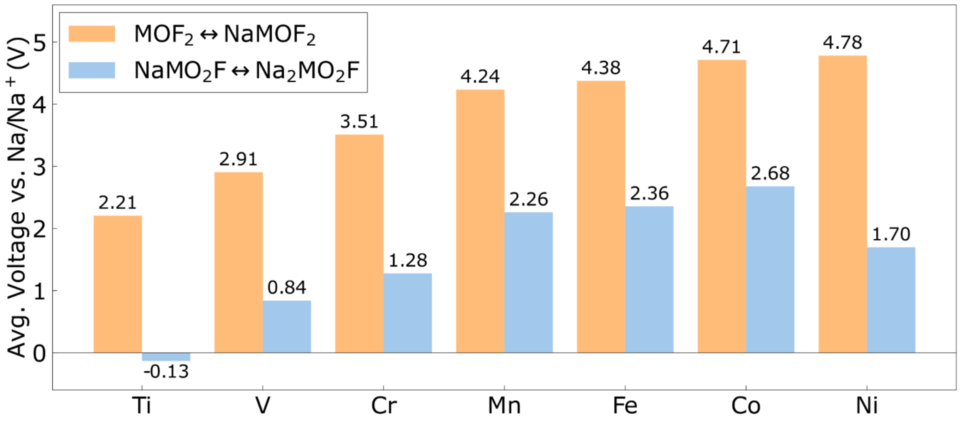

Figure 5. Calculated average Na (de)intercalation voltages (in V), versus Na/Na^+, in F-rich (orange bars) and O-rich (blue bars) TMOFs considered.

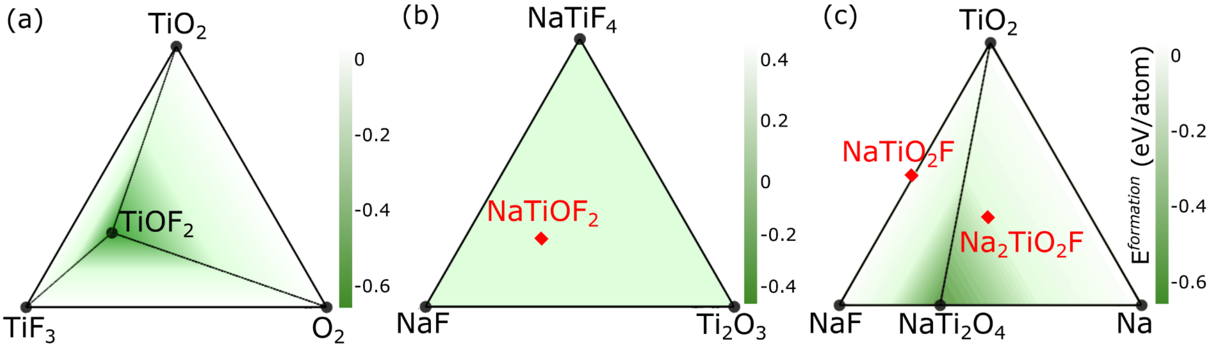

Figure 6. Ternary projections of the Na−Ti−O−F phase diagram to visualize (a) $TiOF_2$, (b) $NaTiOF_2$, and (c) $NaTiO_2F$ and Na_2TiO_2F. In each panel, the green-to-white background represents $E^{formation}$, while the red diamonds indicate meta/instability ($E^{hull} > 0$). Black circles indicate stable compositions and black lines are tie-lines.

1.059,[57] which implies that F-rich $NaMOF_2$ with M as Cr, Mn, and Ni, and O-rich $NaMO_2F$ and Na_2MO_2F with M as Ni have been incorrectly classified. For Li-TMOF stoichiometries, all Li_2MOF_2, $LiTiO_2F$, and $LiVO_2F$ have $t < 0.825$ (Table S7), showing their possibility to form ilmenite structure[57] ($R\bar{3}$) which is in line with the observation of the rhombohedral structure maintained during the intercalation reaction of VO_2F ↔ $LiVO_2F$.[28,29] However, $R3c$ $LiVO_2F$ irreversibly transitions to $Pm\bar{3}m$ Li_2VO_2F[28,29] upon lithiation which might contradict the labeling based on t.

In the case of calculated τ values (Figure 4b), we observe $NaMO_2F$ with M = Ti, V, and Fe lie below the threshold $\tau = 4.18$, but M = Cr, Mn, Co, and Ni lie above 4.18, which suggests that τ is categorizing $NaCrO_2F$, $NaMnO_2F$, and $NaCoO_2F$ perovskites with the $P2/b$ ground state structure as a nonperovskite, in contrast to the labeling by t. Given that τ is a more accurate labeler of perovskite compositions than t, we expect some of the Na-containing O-rich perovskites (i.e., $NaMO_2F$ compositions) to not crystallize in a perovskite structure. On the other hand, all $NaMOF_2$ and Na_2MO_2F compositions have $\tau < 4.18$, similar to t observations for $NaMOF_2$ and Na_2MO_2F with $Pbnm$ and $P2/b$ groundstates. For Li-TMOF stoichiometries, τ predicts none of the Li-containing TMOF compositions to be a perovskite former (Table S7), partly consistent with the experimental observations of disordered rocksalt or amorphized structures for several Li-TMOFs.[27,30,33,34] Nevertheless, both t and τ have been developed strictly for ABO_3 compositions and primarily to predict their polymorphic stabilities (Figure 3). Since, our chosen F-rich and O-rich oxyfluorides are not true ABO_3 stoichiometries, particularly the Na_2MO_2F compositions, we have quantified the true thermodynamic (in)stability of the perovskite compositions considered using our calculated E^{hull} data (see sections below, Figures 6 and 7).

Average Voltages. Figure 5 depicts the calculated average voltages for Na (de)intercalation, versus Na/Na^+, into the ground state polymorphs of F-rich MOF_2 (orange bars) and of O-rich $NaMO_2F$ (blue bars). The extent of Na (de)-intercalation considered in both F-rich and O-rich perovkistes are one Na per f.u., corresponding to MOF_2 ↔ $NaMOF_2$ and $NaMO_2F$ ↔ Na_2MO_2F, respectively. Expectedly, we find the F-rich perovskites to exhibit consistently higher average voltages than the corresponding O-rich perovskites, which can be attributed to the greater inductive effect of F^- compared to O^{2-}.[20] Indeed, fluorine's inductive effect causes an increase in the average voltage of ≥2 V for all TMs (except Mn at a 1.98 V increase), with the increase in Ni being the highest at 3.08 V.

In both the F-rich and the O-rich perovskites, there is a monotonic increase in voltages along the 3d series, with the values increasing from 2.21 V (in Ti) to 4.78 V (Ni) in the F-rich and from −0.13 V (Ti) to 2.68 V (Co) in the O-rich perovskites. The monotonic trends in voltages can be largely attributed to the corresponding trends in standard reduction potentials of the TMs.[68] The dip in voltage from Co to Ni in O-rich perovskites can be primarily attributed to cooperative Jahn−Teller distortion in the Ni-perovskite, which results in larger deviations in the lattice parameters (see compiled b/a and c/a ratios in Mn- and Ni-perovskites in Table S6).

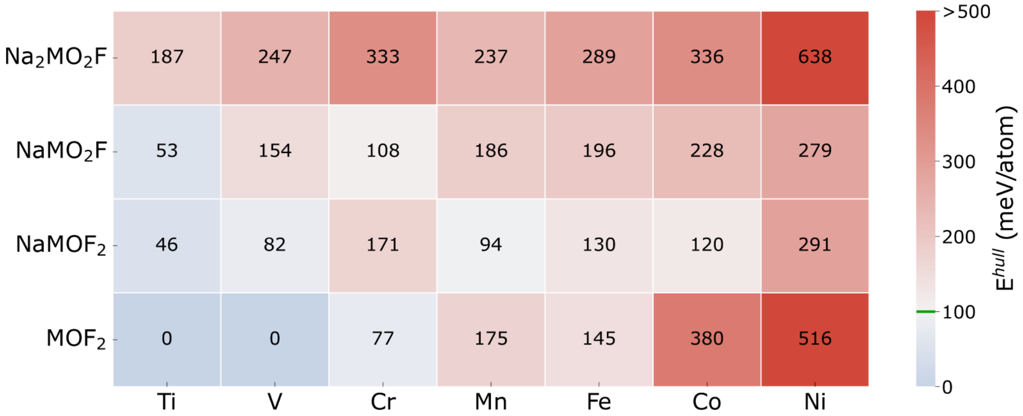

Figure 7. Calculated E^{hull} for charged and discharged F-rich TMOFs (bottom two rows) and O-rich TMOFs (top two rows). Each column represents a 3*d* TM, while the E^{hull} for each compound is indicated by using text annotations within each square. The green line on the legend bar indicates the 100 meV/atom synthesizability threshold considered in this work.

Interestingly, the average intercalation voltage in the O-rich Ti-perovskite exhibits a negative value (−0.13 V), indicating the nonspontaneity of Na-intercalation in this system. This is because the intercalated Na_2TiO_2F is thermodynamically unstable, with Na metal being one of the decomposition products (see Figure 6).

Given the electrolyte stability windows of liquid electrolytes in NIBs typically span up to 4.8 V vs Na/Na$^+$,[69,70] we find all perovskites considered in this work to be suitable as NIB electrodes. The low average voltages of several O-rich perovskites, including V, Cr, Mn, and Fe (<2.5 V), and $TiOF_2$, make these systems more suitable as possible negative electrode candidates (anodes) than cathodes in a NIB. Thus, based on the voltage data alone, we find the Mn-, Fe-, Co-, and Ni-based F-rich perovskites to be possible candidates for NIB cathodes.

Since an intercalation reaction can often lead to metastable/unstable products, we can quantify the differences in thermodynamic driving forces between an intercalation reaction and a corresponding "conversion" reaction, following the framework developed by Hannah et al.[71] Thus, we have illustrated a comparison between intercalation and conversion voltages for all perovskites considered in this work in Figure S3. Nevertheless, the practical deployment of any candidate electrode material in NIBs will be highly dependent on their synthesizability (i.e., thermodynamic stability) and rate performance (i.e., Na-ion mobility), which are discussed in the following sections.

Thermodynamic Stability. Upon construction of the quaternary 0 K Na−TM−O−F convex hulls, we plotted pseudoternary slices (or projections) of the quaternary phase diagram for each TM for the ease of visualization. For instance, ternary projections of the Na−Ti−O−F system is displayed in Figure 6, while the ternary projections for the remaining TM systems are compiled in Figure S4. The background colors in all panels (shades of green) of Figure 6 indicate the energy of formation ($E^{\mathrm{formation}}$), calculated with respect to the terminating compositions of the ternary projections. Stable compounds within the ternary projections are indicated by black circles. Metastable/unstable compounds are indicated by red diamonds. For each metastable/unstable compound among the TMOFs considered, the set of decomposition products (i.e., stable compounds that a metastable/unstable compound is thermodynamically driven to decompose into) is compiled in Table S8.

For visualizing the $TiOF_2$ composition in the Ti-quaternary, we used a ternary projection terminated by TiO_2, TiF_3, and O_2 (see Figure 6a). Similarly, for visualizing $NaTiOF_2$, we used the $NaTiF_4$−NaF−Ti_2O_3 ternary projection (Figure 6b). Both $NaTiO_2F$ and Na_2TiO_2F can be captured within the TiO_2−NaF−Na projection (Figure 6c). Importantly, Figure 6 indicates that $TiOF_2$ is thermodynamically stable (E^{hull} = 0 meV/atom), while $NaTiOF_2$ and $NaTiO_2F$ are metastable with E^{hull} of 46 and 53 meV/atom, respectively, which are below the 100 meV/atom threshold. Also, Na_2TiO_2F is unstable with E^{hull} of 187 meV/atom. Notably, Na metal is one of the decomposition products for the unstable Na_2TiO_2F (Figure 6c), which explains the calculated negative intercalation voltage for the $NaTiO_2F \leftrightarrow Na_2TiO_2F$ reaction (Figure 5).

The heatmap depicted in Figure 7 compiles the E^{hull} data of all charged and discharged O-rich and oxo-rich perovskites considered. Blue squares indicate stable/metastable compounds, while red squares indicate unstable compounds. The text annotations within each square represent the E^{hull} in meV/atom for the corresponding compound. Significantly, we find only $TiOF_2$ and VOF_2 to be thermodynamically stable (i.e., E^{hull} = 0 meV/atom) among all the TMOFs considered. This is in agreement with experimental reports that have synthesized $TiOF_2$[27] and VOF_2.[72] All charged and discharged compositions of Fe-, Co-, and Ni-based TMOFs are unstable, with E^{hull} greater than the synthesizability threshold of 100 meV/atom, citing the high unsuitability of such compositions as NIB electrodes. Moreover, all O-rich perovskites, except $NaTiO_2F$, exhibit E^{hull} > 100 meV/atom, highlighting their high instabilities. Note that tolerance factor estimates, as depicted in Figure 4, do not capture the calculated (in)stability trends accurately since they are designed to predict polymorphic stabilities (Figure 3) and not thermodynamic stabilities, thus signifying the importance of constructing 0 K convex hulls and computing the resulting E^{hull} values.

While it is good for an electrode to have thermodynamically stable charged and discharged states to avoid any irreversible decomposition or conversion reactions during an electrochemical cycle, topotactic (de)intercalation is often possible with metastable charged and discharged states as well.[71,73−75] Thus, compositions that lie within the E^{hull} threshold of 100 meV/atom can be considered as possible electrodes. Given our

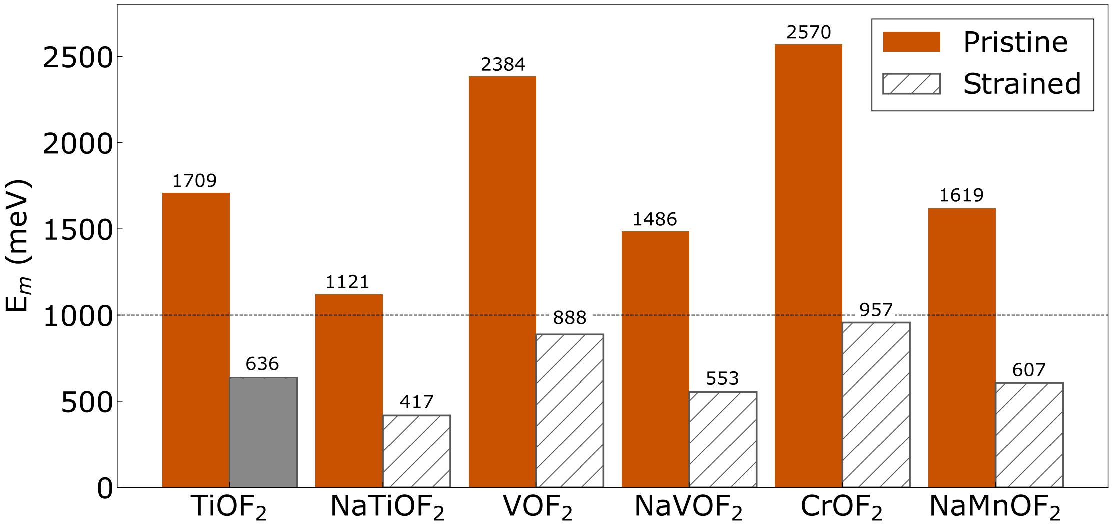

Figure 8. GGA-calculated E_m of pristine (solid orange bars) and strained (solid gray or hashed bars) candidate compositions. The horizontal dotted line indicates a threshold E_m of 1000 meV.

stability data, the possible structures that can be considered as NIB electrodes include $TiOF_2$−$NaTiOF_2$, VOF_2−$NaVOF_2$, $CrOF_2$, and $NaMnOF_2$, and the ease of Na-ion mobility within these frameworks will further determine their suitability. Note that the high instabilities of $NaCrOF_2$ and $MnOF_2$ may limit the Na insertion/extraction capacity in these electrodes, compared to the charged−discharged pairs of $TiOF_2$−$NaTiOF_2$ and VOF_2−$NaVOF_2$. Although we find $NaTiO_2F$ to be metastable, we did not calculate Na E_m within this structure given the negative average intercalation voltage associated with Na_2TiO_2F formation.

Ionic Mobility. For the candidate compositions identified via our voltage and stability calculations, we estimated the Na E_m via the vacancy-mediated mechanism and compiled the values in Figure 8. Barriers calculated in regular TMOF compositions are represented by solid orange bars in Figure 8, while barriers calculated in strained compositions (vide infra) are indicated by solid gray or hatched bars. We used a threshold value of 1000 meV for the E_m, indicated by the dotted black line in Figure 8, to represent an electrode material that can be used under reasonable electrochemical conditions, similar to our previous works.[74,76] Thus, electrodes that exhibit $E_m \leq 1000$ meV are considered candidates for further experimental exploration. Notably, all short-listed TMOF compositions exhibit barriers that are above the 1000 meV threshold in their pristine state. Only $NaTiOF_2$, with a barrier of 1121 meV, is close to the 1000 meV threshold, with other compositions exhibiting significantly higher E_m, including $NaVOF_2$ (1486 meV), $NaMnOF_2$ (1619 meV), $TiOF_2$ (1709 meV), VOF_2 (2384 meV), and $CrOF_2$ (2570 meV).

Introducing strain in an electrode can often lead to lowering of E_m and consequent increasing in ionic mobility.[77−79] Thus, to examine whether the identified TMOFs can reasonably function as NIB electrodes under strain, we introduced a homogeneous tensile strain of 5% across all lattice parameters of $TiOF_2$ and evaluated the Na-E_m values using the GGA-based NEB. To ensure that the tensile strain is maintained during structural relaxation, we restricted the relaxation of the end points to only include changes in ionic positions. Importantly, the strain introduction significantly reduced the E_m to 636 meV (i.e., by 62.8%) compared to pristine-$TiOF_2$, as shown by the solid gray bar in Figure 8.

Assuming similar reductions in calculated E_m with strain addition in other TMOFs (i.e., by 62.8% compared to the pristine-case), we estimate the barriers in strained $NaTiOF_2$, VOF_2, $NaVOF_2$, $CrOF_2$, and $NaMnOF_2$ to be 417, 888, 553, 957, and 607 meV, respectively (see hashed bars in Figure 8). Thus, all TMOFs identified using our voltage and stability criteria may exhibit reasonable Na-ionic mobility, provided that a homogeneous strain is introduced within the materials. In practice, lattice expansion can be achieved through doping,[80,81] heat/mechanical treatment,[82,83] and/or epitaxially, such as in the case of thin film electrodes.[78,84] Note that introducing strain and maintaining it during electrochemical cycling may come at the cost of the energy density of the eventual battery. Thus, we expect $TiOF_2$−$NaTiOF_2$, VOF_2−$NaVOF_2$, $CrOF_2$, and $NaMnOF_2$ to be NIB electrodes worth exploring experimentally, if utilized under strained electrode configurations and thin film batteries.

DISCUSSION

In this work, we performed first-principles calculations to explore the scope of 3*d* TM-based F- and O-rich perovskite oxyfluorides (Na_xMOF_2 and $Na_{1+x}MO_2F$, $x = 0$−1) as NIB electrodes. Using a structural template based workflow, we identified the ground state polymorphs of the charged MOF_2 and $NaMO_2F$ compositions (M = Ti, V, Cr, Mn, Fe, Co, or Ni) among six possible space groups commonly adopted by perovskites. Subsequently, we introduced Na to create the corresponding discharged perovskite compositions, namely, $NaMOF_2$ and Na_2MO_2F, and evaluted the average Na (de)intercalation voltages, 0 K thermodynamic stabilities in all perovskites, and Na-ion mobility in a selected set of candidate perovskites. Based on our voltage, stability, and mobility calculations, we identify six perovskite compositions, namely, $TiOF_2$−$NaTiOF_2$, VOF_2−$NaVOF_2$, $CrOF_2$, and $NaMnOF_2$ to hold some promise, alongside challenges, as NIB electrodes, if used in strained configurations and/or in thin film batteries.

During the process of enumerating possible structures for the charged perovskites, we only considered a maximum of 16 lowest electrostatic energy configurations within each space group and identified the ground state configuration among these structures as the one with the lowest DFT total energy (per f.u.). Note that the choice of the 16 lowest electrostatic energy structures (per space group) is an approximation, and there is always a nonzero chance of encountering the "true" ground state beyond this choice. Using our criteria of a maximum of 16 structures per space group contributes to a total of 72 structures per perovskite composition (i.e., $16 \times 4 + 5 + 3$), which in turn adds up to 1008 structures over all TMs considered and over both O-rich and F-rich compositions, which by itself represents a significant computational expense. Nevertheless, even if the "true" ground state is beyond the set of configurations we have considered here, we expect it to exhibit a lower energy, of the order of ∼10 meV/f.u., compared to the ground state that we have identified, which will only cause a marginal change to the voltage (∼10 mV) and stability ($E^{\text{hull}} \pm 10$ meV/f.u.) predictions.

Another approximation in our structure generation workflow is the identification of ground state configurations at the charged perovskite compositions, followed by the addition of Na to the lowest-energy charged structure to obtain the discharged structure. We could have followed a similar procedure of ground state identification using the discharged composition instead of the charged composition. Our choice of the charged perovskite composition for ground state identification was motivated largely by experimental reports on TMOFs in LIBs, wherein, Li was typically inserted into charged TMOF compositions.[27,28] Thus, the TMOF composition was synthesized first, followed by Li discharge to obtain the discharged state. Considering the ground state configuration at the discharged state may lead to qualitatively different results in terms of average voltages, 0 K stability, and Na-ionic mobility. But considering a workflow along the discharged compositions represents a significant computational effort, which we plan to take up as future work.

In this work, we have restricted our investigation to the 3*d* series despite the possibility that oxyfluoride frameworks may form with second-row TMs (such as Mo and Nb).[27,85,86] Note that TMOFs with 4*d* TMs are likely to exhibit lower Na intercalation voltages compared to the corresponding 3*d* TMs, similar to trends observed in phosphate-based polyanionic cathodes. For example, $Nb_2(PO_4)_3 \leftrightarrow Na_3Nb_2(PO_4)_3$ exhibits a lower 1.46 V,[87] compared to the analogous $NaV_2(PO_4)_3 \leftrightarrow Na_3V_2(PO_4)_3$ that exhibits a higher 3.4 V.[88] A similar trend is also observed on comparing the Mo ($NaMo_2(PO_4)_3 \leftrightarrow Na_3Mo_2(PO_4)_3$; 2.45 V),[89] to the Cr ($NaCr_2(PO_4)_3 \leftrightarrow Na_3Cr_2(PO_4)_3$; 4.5 V),[90] phosphate. Nevertheless, 4*d* perovskite-based TMOFs are worth exploring as potential NIB anodes.

We particularly chose the O/F ratios of 1:2 and 2:1 in this work to facilitate the $M^{4+/3+}$ redox-couple during Na (de)intercalation. Note that this choice of O:F ratios not only maximizes the voltage (via $M^{4+/3+}$ redox-activity) but also maximizes capacity by enabling the theoretical exchange of 1 mol of Na per TMOF formula unit. Indeed, O:F ratios other than 1:2 or 2:1 will introduce mixed oxidation states of M at the discharged and charged compositions, which will limit the theoretical capacity. Moreover, the computational modeling of O:F ratios other than 1:2 or 2:1 necessitates the usage of larger perovskite supercells (for each space group considered), which significantly increases computational cost per calculation and also increases the number of unique configurations that we will have to sample to arrive at the ground state configuration. In any case, we have only sampled a sliver of possible chemistries that can be accessed within the TMOF chemical space, and we aim to explore other O:F ratios as part of follow-up work.

For all SCAN+*U* calculations, we used the *U* value derived from TM oxides since the oxide-based *U* better reproduced the experimentally determined voltages for Li-intercalation in TMOFs, such as $VO_2F \leftrightarrow LiVO_2F$ and $TiOF_2 \leftrightarrow Li_{0.5}TiOF_2$.[27,28] Hence, we did not tailor our *U* values specifically for oxyfluorides. More experimental data will be needed to verify if such tailored *U* values will yield more accurate predictions. Additionally, we initialized all our TMs in their corresponding ferromagnetic high-spin configurations and did not consider possible magnetic/spin orderings due to their computational complexity, which may have marginally affected the set of ground states that we obtained. Also, SCAN+*U* is known to overestimate intercalation voltages and meta/instability of compounds,[91] which is also a reason for us to consider a fairly large threshold ($E^{\text{hull}} \leq 100$ meV/atom) for synthesizability.

The metastable compositions of $NaTiOF_2$, $NaVOF_2$, and $NaMnOF_2$ are predicted to decompose to more stable oxides and fluorides. For example, $NaTiOF_2$ should decompose into Ti_2O_3, $NaTiF_4$, and NaF (see Table S8), all of which are solid phases consisting of a single anion (i.e., oxygen or fluorine). This type of solid-state decomposition reaction that involves phase separation within the anionic entity (i.e., formation of oxides and fluorides from oxyfluorides) is expected to be slow, since this will involve the diffusion of anionic species in addition to the cations.[92−94] Thus, we expect $NaTiOF_2$, $NaVOF_2$, and $NaMnOF_2$ to remain metastable under typical electrochemical conditions. Additionally, if decomposition indeed occurs, electrochemically active decomposition products like Ti_2O_3,[95] $NaTiF_4$,[96] V_2O_3,[23] Na_3VF_6,[23] or Na_3MnF_6,[97] which have open channels for Na migration, may participate as (de)intercalation frameworks, thus contributing to electrochemical activity. Hence, careful characterization of the electrochemical performance of TMOFs may be necessary to ensure that any observed activity is indeed due to the exchange of Na with the TMOF framework.

In the case of metastable-$CrOF_2$, the structure is predicted to form O_2 gas as a decomposition product (Table S8), which can entropically drive the decomposition reaction. While O_2 evolution during synthesis can be mitigated by increasing the partial pressure of O_2,[98,99] preventing O_2 evolution during electrochemical cycling may be challenging.[100] Moreover, we observed all of the discharged phases of the O-rich oxyfluorides (Na_2MO_2F) are unstable with significantly higher E^{hull} than 100 meV/atom. Perhaps, the increase in electrostatic repulsion due to inserting two Na ions into the A-site of the perovskite framework might have affected stability and is reflected by the high E^{hull} values observed in Na_2MO_2F, which further supports the idea that these materials may not be practically viable.

We used a reasonably high threshold for ionic mobility ($E_m \leq 1000$ meV[74]) to identify candidates partly due to the limited literature on Na-ion mobility within crystalline ordered oxyfluorides. Moreover, the addition of F^- to oxides can result in a reduction of Na^+ mobility due to more ionic Na−F bonds than Na−O, similar to observations of reduction in Li-mobility in F-doped oxide-based disordered rocksalts.[101,102] Importantly, our calculations indicated that only $NaTiOF_2$ (E_m = 1121 meV) came close to the threshold used, with all other oxyfluorides considered exhibiting significantly high E_m for Na-motion. We observe that Na^+ has to migrate via a tetrahedral void sandwiched between two Na−O−F polyhedra in the perovskites considered, i.e., *Pbnm*-based $TiOF_2$−$NaTiOF_2$ and VOF_2−$NaVOF_2$, and $R\bar{3}c$-based $CrOF_2$ and $NaMnOF_2$, which may contribute to the observed high E_m in these structures.[103] However, introducing a homogeneous strain (∼5%) within the lattice can significantly reduce the E_m (by ∼60%), as demonstrated for the case of $TiOF_2$, due to the expansion of the transition state (see Figure S6). Thus, TMOFs can exhibit reasonable rate performance under lattice strain. However, the need to maintain the strained structure may limit the applicability of TMOFs to low power and/or thin film batteries that are typically used in Internet-of-things applications and wearable electronics.

Considering the oxyfluoride compositions of Na_xMOF_2 and $Na_{1+x}MO_2F$ was primarily motivated by the availability of the $M^{4+/3+}$ redox couple, which is exhibited by several 3*d* TMs, quite reversibly. Our work can be extended to other fluorine-added compositions, such as F-substituted oxides, phosphates, sulfates, and pyrophosphates. Indeed, high voltages and capacities with Na (de)intercalation have already been reported in fluorophosphates.[104−106] Therefore, we are hopeful that our research lays the foundation for exploring other promising compositions for NIB electrodes within and beyond the chemical space of oxyfluorides.

CONCLUSION

NIBs, which represent an alternative technological pathway to state-of-the-art LIBs in energy storage technology, require novel materials to improve the energy and power densities so that NIBs compete better with LIBs. Here, we explored the chemical space of perovskite-based TMOFs, considering both the O-rich and F-rich compositions as possible Na-ion intercalation hosts. Specifically, we performed DFT-based calculations on Na_xMOF_2 and $Na_{1+x}MO_2F$ ($x = 0$−1), where M = Ti, V, Cr, Mn, Fe, Co, or Ni, evaluating the ground state polymorphs, average Na (de)intercalation voltages, 0 K stabilities, and Na^+ mobilities. We found that F-rich perovskites exhibit higher voltages than O-rich compositions due to the stronger inductive effect of F^-. In terms of stability, only $TiOF_2$ and VOF_2 were stable, while other compositions, including $NaTiOF_2$, $NaVOF_2$, $CrOF_2$, and $NaMnOF_2$ were metastable ($E^{hull} \leq 100$ meV/atom). However, all stable and metastable TMOFs exhibited a high E_m (≥1000 meV) for Na^+ motion in their pristine states. Nevertheless, introducing a 5% homogeneous tensile strain causes the E_m to drop by ∼60% compared to the pristine state, suggesting that the TMOFs may have applications in thin film batteries and in strained electrode configurations. Our study represents a systematic computational exploration of the oxyfluoride chemical space, which we hope will reinvigorate research in these chemistries for NIBs and beyond.

ASSOCIATED CONTENT

Data Availability Statement

The data that support the findings of this study are openly available at our GitHub repository.

Supporting Information

The Supporting Information is available free of charge at https://pubs.acs.org/doi/10.1021/acs.chemmater.4c02374.

Details of PAW potentials used, description of site determination for introducing additional Na in perovskites, compilation of 0 K phase diagrams, conversion voltages, and the associated stability data, and all calculated MEPs (PDF)

AUTHOR INFORMATION

Corresponding Author

Gopalakrishnan Sai Gautam − *Department of Materials Engineering, Indian Institute of Science, Bengaluru 560012, India*; orcid.org/0000-0002-1303-0976; Email: saigautamg@iisc.ac.in

Author

Debolina Deb − *Department of Materials Engineering, Indian Institute of Science, Bengaluru 560012, India*

Complete contact information is available at: https://pubs.acs.org/10.1021/acs.chemmater.4c02374

Notes

The authors declare no competing financial interest.

ACKNOWLEDGMENTS

G.S.G. acknowledges financial support from the Indian Institute of Science (IISc) and support from the Science and Engineering Research Board (SERB) of Government of India, under sanction numbers SRG/2021/000201 and IPA/2021/000007. D.D. thanks the Ministry of Human Resource Development, Government of India, for financial assistance. The authors acknowledge the computational resources provided by the Supercomputer Education and Research Centre (SERC), IISc. A portion of the calculations in this work used computational resources of the supercomputer Fugaku provided by RIKEN through the HPCI System Research Project (project ID: hp220393). We acknowledge the National Supercomputing Mission (NSM) for providing computing resources of "PARAM Siddhi-AI", under the National PARAM Supercomputing Facility (NPSF), C-DAC, Pune, and the resources of "Param Utkarsh" at the CDAC Knowledge Park, Bengaluru. Both PARAM Siddhi-AI and PARAM Utkarsh are implemented by CDAC and supported by the Ministry of Electronics and Information Technology (MeitY) and Department of Science and Technology (DST), Government of India. The authors gratefully acknowledge the computing time provided in them on the high-performance computer noctua1 and noctua2 at the NHR Center PC2. This was funded by the Federal Ministry of Education and Research and the state governments participating on the basis of the resolutions of the GWK for the national high-performance computing at universities (www.nhr-verein.de/unsere-partner). The computations for this research were performed using computing resources under project hpc-prf-emdft and hpc-prf-desal.

REFERENCES

(1) Chayambuka, K.; Mulder, G.; Danilov, D. L.; Notten, P. H. From li-ion batteries toward Na-ion chemistries: challenges and opportunities. *Adv. Energy Mater.* **2020**, *10*, 2001310.

(2) Vaalma, C.; Buchholz, D.; Weil, M.; Passerini, S. A cost and resource analysis of sodium-ion batteries. *Nat. Rev. Mater.* **2018**, *3*, 18013.

(3) Zhang, J.; Wang, W.; Wang, W.; Wang, S.; Li, B. Comprehensive review of P2-type $Na_{2/3}Ni_{1/3}Mn_{2/3}O_2$, a potential cathode for practical application of Na-ion batteries. *ACS Appl. Mater. Interfaces* **2019**, *11*, 22051−22066.

(4) Xiao, J.; Li, X.; Tang, K.; Wang, D.; Long, M.; Gao, H.; Chen, W.; Liu, C.; Liu, H.; Wang, G. Recent progress of emerging cathode materials for sodium ion batteries. *Mater. Chem. Front.* **2021**, *5*, 3735−3764.

(5) Kim, S.-W.; Seo, D.-H.; Ma, X.; Ceder, G.; Kang, K. Electrode materials for rechargeable sodium-ion batteries: potential alternatives to current lithium-ion batteries. *Adv. Energy Mater.* **2012**, *2*, 710−721.

(6) Rudola, A.; Sayers, R.; Wright, C. J.; Barker, J. Opportunities for moderate-range electric vehicles using sustainable sodium-ion batteries. *Nat. Energy* **2023**, *8*, 215−218.

(7) Barker, J.; Wright, C. *Storage and/or transportation of sodium-ion cells*, 2017 WO 2,016,027,082 A1.

(8) Li, X.; Zhang, X.; Lin, W.; Chen, X.; Liu, B.; Yao, S.; Lan, J. *Secondary battery, battery module, battery pack, and electric apparatus*, 2024 US 20,240,047,756 A1.

(9) Hirsh, H. S.; Li, Y.; Tan, D. H.; Zhang, M.; Zhao, E.; Meng, Y. S. Sodium-ion batteries paving the way for grid energy storage. *Adv. Energy Mater.* **2020**, *10*, 2001274.

(10) Wei, F.; Zhang, Q.; Zhang, P.; Tian, W.; Dai, K.; Zhang, L.; Mao, J.; Shao, G. Research progress on layered transition metal oxide cathode materials for sodium ion batteries. *J. Electrochem. Soc.* **2021**, *168*, 050524.

(11) Kim, J. C.; Kwon, D.-H.; Yang, J. H.; Kim, H.; Bo, S.-H.; Wu, L.; Kim, H.; Seo, D.-H.; Shi, T.; Wang, J.; et al. Direct observation of alternating octahedral and prismatic sodium layers in O3-type transition metal oxides. *Adv. Energy Mater.* **2020**, *10*, 2001151.

(12) Deb, D.; Sai Gautam, G. Critical overview of polyanionic frameworks as positive electrodes for Na-ion batteries. *J. Mater. Res.* **2022**, *37*, 3169−3196.

(13) Mariyappan, S.; Wang, Q.; Tarascon, J. M. Will sodium layered oxides ever be competitive for sodium ion battery applications? *J. Electrochem. Soc.* **2018**, *165*, A3714.

(14) Tian, M.; Xu, L.; Yang, Y. Perovskite oxide ferroelectric thin films. *Adv. Electron. Mater.* **2022**, *8*, 2101409.

(15) Ye, S.; Zhu, J.; Zhu, S.; Zhao, Y.; Li, M.; Huang, Z.; Wang, H.; He, J. Design strategies for perovskite-type high-entropy oxides with applications in optics. *ACS Appl. Mater. Interfaces* **2023**, *15*, 47475−47486.

(16) Assirey, E. A. R. Perovskite synthesis, properties and their related biochemical and industrial application. *Saudi Pharm. J.* **2019**, *27*, 817−829.

(17) Fakharuddin, A.; Gangishetty, M. K.; Abdi-Jalebi, M.; Chin, S.-H.; Bin Mohd Yusoff, A. R.; Congreve, D. N.; Tress, W.; Deschler, F.; Vasilopoulou, M.; Bolink, H. J. Perovskite light-emitting diodes. *Nat. Electron.* **2022**, *5*, 203−216.

(18) Sai Gautam, G.; Stechel, E. B.; Carter, E. A. Exploring Ca−Ce−M−O (M= 3d transition metal) oxide perovskites for solar thermochemical applications. *Chem. Mater.* **2020**, *32*, 9964−9982.

(19) Evans, H. A.; Wu, Y.; Seshadri, R.; Cheetham, A. K. Perovskite-related ReO_3-type structures. *Nat. Rev. Mater.* **2020**, *5*, 196−213.

(20) Wang, Y.; Wu, Z.; Azad, F. M.; Zhu, Y.; Wang, L.; Hawker, C. J.; Whittaker, A. K.; Forsyth, M.; Zhang, C. Fluorination in advanced battery design. *Nat. Rev. Mater.* **2024**, *9*, 119−133.

(21) Manthiram, A.; Goodenough, J. Lithium insertion into $Fe_2(SO_4)_3$ frameworks. *J. Power Sources* **1989**, *26*, 403−408.

(22) Padhi, A. K.; Nanjundaswamy, K. S.; Goodenough, J. B. Phospho-olivines as positive-electrode materials for rechargeable lithium batteries. *J. Electrochem. Soc.* **1997**, *144*, 1188.

(23) Yan, G.; Mariyappan, S.; Rousse, G.; Jacquet, Q.; Deschamps, M.; David, R.; Mirvaux, B.; Freeland, J. W.; Tarascon, J.-M. Higher energy and safer sodium ion batteries via an electrochemically made disordered $Na_3V_2(PO_4)_2F_3$ material. *Nat. Commun.* **2019**, *10* (1), 585.

(24) Nguyen, L. H.; Iadecola, A.; Belin, S.; Olchowka, J.; Masquelier, C.; Carlier, D.; Croguennec, L. A combined operando synchrotron X-ray absorption spectroscopy and first-principles density functional theory study to unravel the vanadium redox paradox in the $Na_3V_2(PO_4)_2F_3$−$Na_3V_2(PO_4)_2FO_2$ compositions. *J. Phys. Chem. C* **2020**, *124*, 23511−23522.

(25) Akhtar, M.; Arraghraghi, H.; Kunz, S.; Wang, Q.; Bianchini, M. novel solid-state synthesis route for high voltage $Na_3V_2(PO4)_2F_{3-2y}O_{2y}$ cathode materials for Na-ion batteries. *J. Mater. Chem. A* **2023**, *11*, 25650−25661.

(26) Deng, D. Transition Metal Oxyfluorides for Next-Generation Rechargeable Batteries. *ChemNanomat* **2017**, *3*, 146−159.

(27) Reddy, M.; Madhavi, S.; Rao, G. S.; Chowdari, B. Metal oxyfluorides $TiOF_2$ and NbO_2F as anodes for Li-ion batteries. *J. Power Sources* **2006**, *162*, 1312−1321.

(28) Kuhn, A.; Plews, M. R.; Pérez-Flores, J. C.; Fauth, F.; Hoelzel, M.; Cabana, J.; García-Alvarado, F. Redox Chemistry and Reversible Structural Changes in Rhombohedral VO_2F Cathode during Li Intercalation. *Inorg. Chem.* **2020**, *59*, 10048−10058.

(29) Wang, X.; Lin, Y.-C.; Zhou, H.; Omenya, F.; Chu, I.-H.; Karki, K.; Sallis, S.; Rana, J.; Piper, L. F.; Chernova, N. A.; et al. Structural changes in a high-energy density VO_2F cathode upon heating and Li cycling. *ACS Appl. Energy Mater.* **2018**, *1*, 4514−4521.

(30) Xu, X.; Pi, L.; Marie, J.-J.; Rees, G. J.; Gong, C.; Pu, S.; House, R. A.; Robertson, A. W.; Bruce, P. G. Li_2NiO_2F a new oxyfluoride disordered rocksalt cathode material. *J. Electrochem. Soc.* **2021**, *168*, 080521.

(31) Shirazi Moghadam, Y.; El Kharbachi, A.; Hu, Y.; Wang, K.; Belin, S.; Fichtner, M. Na-Rich Disordered Rock Salt Oxyfluoride Cathode Materials for Sodium Ion Batteries. *ACS Mater. Lett.* **2023**, *5*, 125−132.

(32) Pérez-Flores, J. C.; Villamor, R.; Ávila-Brande, D.; Amores, J. M. G.; Morán, E.; Kuhn, A.; García-Alvarado, F. VO_2F: a new transition metal oxyfluoride with high specific capacity for Li ion batteries. *J. Mater. Chem. A* **2015**, *3*, 20508−20515.

(33) Chen, R.; Maawad, E.; Knapp, M.; Ren, S.; Beran, P.; Witter, R.; Hempelmann, R. Lithiation-driven structural transition of VO_2F into disordered rock-salt Li_xVO_2F. *RSC Adv.* **2016**, *6* (6), 65112−65118.

(34) Astrova, E. V.; Ulin, V. P.; Parfeneva, A. V.; Li, G. V.; Yagovkina, M. A.; Lozhkina, D. A.; Krasilin, A. A.; Tomkovich, M. V.; Rumyantsev, A. M. Titanium Oxyfluoride as a Material for Negative Electrodes of Lithium-Ion Batteries. *Int. J. Mol. Sci.* **2023**, *24*, 4968.

(35) Kitajou, A.; Zhao, L.; Nagano, R.; Inoishi, A.; Kobayashi, E.; Okada, S. Electrochemical performance and thermal stability of iron oxyfluoride (FeOF) for sodium-ion batteries. *Batteries* **2018**, *4*, 68.

(36) Clément, R.; Lun, Z.; Ceder, G. Cation-disordered rocksalt transition metal oxides and oxyfluorides for high energy lithium-ion cathodes. *Energy Environ. Sci.* **2020**, *13*, 345−373.

(37) Ye, J.; Shea, P.; Baumgaertel, A. C.; Bonev, S. A.; Biener, M. M.; Bagge-Hansen, M.; Wang, Y. M.; Biener, J.; Wood, B. C. Amorphization as a pathway to fast charging kinetics in atomic layer deposition-derived titania films for lithium ion batteries. *Chem. Mater.* **2018**, *30*, 8871−8882.

(38) Hellenbrandt, M. The inorganic crystal structure database (ICSD)—present and future. *Crystallogr. Rev.* **2004**, *10*, 17−22.

(39) Culbertson, C. M.; Flak, A. T.; Yatskin, M.; Cheong, P. H.-Y.; Cann, D. P.; Dolgos, M. R. Neutron Total Scattering Studies of Group II Titanates ($ATiO_3$, A^{2+} = Mg, Ca, Sr, Ba). *Sci. Rep.* **2020**, *10*, 3729.

(40) Shannon, R. D. Revised effective ionic radii and systematic studies of interatomic distances in halides and chalcogenides. *Acta Crystallogr., Sect. A: Found. Adv.* **1976**, *32*, 751−767.

(41) Ali, R.; Yashima, M. Space group and crystal structure of the Perovskite $CaTiO_3$ from 296 to 1720K. *J. Solid State Chem.* **2005**, *178*, 2867−2872.

(42) Heubner, C.; Heiden, S.; Schneider, M.; Michaelis, A. In-situ preparation and electrochemical characterization of submicron sized $NaFePO_4$ cathode material for sodium-ion batteries. *Electrochim. Acta* **2017**, *233*, 78−84.

(43) Chu, I.-H.; Roychowdhury, S.; Han, D.; Jain, A.; Ong, S. P. Predicting the volumes of crystals. *Comput. Mater. Sci.* **2018**, *146*, 184−192.

(44) Ewald, P. P. Die Berechnung optischer und elektrostatischer Gitterpotentiale. *Ann. Phys.* **1921**, *369*, 253−287.

(45) Kresse, G.; Furthmüller, J. Efficiency of ab-initio total energy calculations for metals and semiconductors using a plane-wave basis set. *Comput. Mater. Sci.* **1996**, *6*, 15−50.

(46) Kresse, G.; Furthmüller, J. Efficient iterative schemes for ab initio total-energy calculations using a plane-wave basis set. *Phys. Rev. B* **1996**, *54*, 11169.

(47) Kresse, G.; Joubert, D. From ultrasoft pseudopotentials to the projector augmented-wave method. *Phys. Rev. B* **1999**, *59*, 1758.

(48) Blöchl, P. E. Projector augmented-wave method. *Phys. Rev. B* **1994**, *50*, 17953.

(49) Gautam, G. S.; Carter, E. A. Evaluating transition metal oxides within DFT-SCAN and SCAN+*U* frameworks for solar thermochemical applications. *Phys. Rev. Mater.* **2018**, *2*, 095401.

(50) Long, O. Y.; Gautam, G. S.; Carter, E. A. Evaluating optimal U for 3 d transition-metal oxides within the SCAN+*U* framework. *Phys. Rev. Mater.* **2020**, *4*, 045401.

(51) Swathilakshmi, S.; Devi, R.; Sai Gautam, G. Performance of the r^{2}SCAN functional in transition metal oxides. *J. Chem. Theory Comput.* **2023**, *19*, 4202−4215.

(52) Dudarev, S. L.; Botton, G. A.; Savrasov, S. Y.; Humphreys, C.; Sutton, A. P. Electron-energy-loss spectra and the structural stability of nickel oxide: An LSDA+*U* study. *Phys. Rev. B* **1998**, *57*, 1505.

(53) Anisimov, V. I.; Zaanen, J.; Andersen, O. K. Band theory and Mott insulators: Hubbard *U* instead of Stoner I. *Phys. Rev. B* **1991**, *44*, 943.

(54) Sun, J.; Ruzsinszky, A.; Perdew, J. P. Strongly constrained and appropriately normed semilocal density functional. *Phys. Rev. Lett.* **2015**, *115*, 036402.

(55) Monkhorst, H. J.; Pack, J. D. Special points for Brillouin-zone integrations. *Phys. Rev. B* **1976**, *13*, 5188.

(56) Hunter, J. D. Matplotlib: A 2D graphics environment. *Comput. Sci. Eng.* **2007**, *9*, 90−95.

(57) Goldschmidt, V. M. Die gesetze der krystallochemie. *Naturwissenschaften* **1926**, *14*, 477−485.

(58) Albrecht, E. K.; Karttunen, A. J. Investigation on the predictive power of tolerance factor *τ* for A-site double perovskite oxides. *Dalton Trans.* **2023**, *52*, 12461−12469.

(59) Li, W.; Ionescu, E.; Riedel, R.; Gurlo, A. Can we predict the formability of perovskite oxynitrides from tolerance and octahedral factors? *J. Mater. Chem. A* **2013**, *1*, 12239−12245.

(60) Bartel, C. J.; Sutton, C.; Goldsmith, B. R.; Ouyang, R.; Musgrave, C. B.; Ghiringhelli, L. M.; Scheffler, M. New tolerance factor to predict the stability of perovskite oxides and halides. *Sci. Adv.* **2019**, *5* (2), No. eaav0693.

(61) Gautam, G. S.; Canepa, P. *Magnesium Batteries: research and Applications*; The Royal Society of Chemistry, 2019.

(62) Balachandran, P. V.; Emery, A. A.; Gubernatis, J. E.; Lookman, T.; Wolverton, C.; Zunger, A. Predictions of new ABO_3 perovskite compounds by combining machine learning and density functional theory. *Phys. Rev. Mater.* **2018**, *2*, 043802.

(63) Aydinol, M.; Kohan, A.; Ceder, G. Ab initio calculation of the intercalation voltage of lithium-transition-metal oxide electrodes for rechargeable batteries. *J. Power Sources* **1997**, *68*, 664−668.

(64) Sheppard, D.; Terrell, R.; Henkelman, G. *Optimization methods for finding minimum energy paths*; The Journal of chemical physics, 2008; Vol. *128*.

(65) Henkelman, G.; Jóhannesson, G.; Jónsson, H. *Methods for finding saddle points and minimum energy paths*; Theoretical methods in condensed phase chemistry, 2002; pp. 269−302.

(66) Perdew, J. P.; Burke, K.; Ernzerhof, M. Generalized gradient approximation made simple. *Phys. Rev. Lett.* **1996**, *77*, 3865.

(67) Devi, R.; Singh, B.; Canepa, P.; Sai Gautam, G. Effect of exchange-correlation functionals on the estimation of migration barriers in battery materials. *Npj Comput. Mater.* **2022**, *8* (1), 160.

(68) Vanysek, P. Electrochemical series. *CRC handbook of chemistry and physics* **2000**, *8*, 8−33.

(69) Karahan Toprakci, H. A.; Toprakci, O. Recent Advances in New-Generation Electrolytes for Sodium-Ion Batteries. *Energies* **2023**, *16*, 3169.

(70) Wu, F.; Zhu, N.; Bai, Y.; Liu, L.; Zhou, H.; Wu, C. Highly safe ionic liquid electrolytes for sodium-ion battery: wide electrochemical window and good thermal stability. *ACS Appl. Mater. Interfaces* **2016**, *8*, 21381−21386.

(71) Hannah, D. C.; Sai Gautam, G.; Canepa, P.; Ceder, G. On the balance of intercalation and conversion reactions in battery cathodes. *Adv. Energy Mater.* **2018**, *8*, 1800379.

(72) Koksbang, R. Lithium battery electrode compositions, 1996 US 5,512,214 A.

(73) Malik, R.; Abdellahi, A.; Ceder, G. A critical review of the Li insertion mechanisms in $LiFePO_4$ electrodes. *J. Electrochem. Soc.* **2013**, *160*, A3179.

(74) Tekliye, D. B.; Kumar, A.; Weihang, X.; Mercy, T. D.; Canepa, P.; Sai Gautam, G. Exploration of NASICON frameworks as calcium-ion battery electrodes. *Chem. Mater.* **2022**, *34*, 10133−10143.

(75) Amatucci, G.; Tarascon, J.; Klein, L. Cobalt dissolution in $LiCoO_2$-based non-aqueous rechargeable batteries. *Solid State Ionics* **1996**, *83*, 167−173.

(76) Lu, W.; Wang, J.; Sai Gautam, G.; Canepa, P. Searching ternary oxides and chalcogenides as positive electrodes for calcium batteries. *Chem. Mater.* **2021**, *33*, 5809−5821.

(77) Wen, K.; Lv, W.; He, W. Interfacial lattice-strain effects on improving the overall performance of micro-solid oxide fuel cells. *J. Mater. Chem. A* **2015**, *3*, 20031−20050.

(78) Tealdi, C.; Heath, J.; Islam, M. S. Feeling the strain: enhancing ionic transport in olivine phosphate cathodes for Li-and Na-ion batteries through strain effects. *J. Mater. Chem. A* **2016**, *4*, 6998−7004.

(79) Jia, M.; Wang, H.; Sun, Z.; Chen, Y.; Guo, C.; Gan, L. Exploring ion migration in Li_2MnSiO_4 for Li-ion batteries through strain effects. *RSC Adv.* **2017**, *7* (7), 26089−26096.

(80) Liao, H.; Xie, L.; Zhang, Y.; Qiu, X.; Li, S.; Huang, Z.; Hou, H.; Ji, X. Mo-doped gray anatase TiO_2: lattice expansion for enhanced sodium storage. *Electrochim. Acta* **2016**, *219*, 227−234.

(81) Sun, J.; Ji, D.; Ye, H.; Yu, B.; Wang, Y.; Ramakrishna, S.; Lu, L. Doping induced hierarchical lattice expansion of cobalt diselenide/carbon nanosheet hybrid for fast and stable sodium storage. *Cell Rep. Phys. Sci.* **2020**, *1*, 100082.

(82) Thomas, S.; Nam, E. B.; Lee, S. U. Atomistic dynamics investigation of the thermomechanical properties and Li diffusion kinetics in *ψ*-graphene for LIB anode material. *ACS Appl. Mater. Interfaces* **2018**, *10*, 36240−36248.

(83) Khan, R.; Yan, W.; Ahmad, W.; Wan, Z.; Hussain, S.; Zeb, A.; Saleem, M. F.; Ling, M.; Liang, C. Role of moderate strain engineering in Nickel Sulfide anode for advanced sodium-ion batteries. *J. Alloys Compd.* **2023**, *963*, 171196.

(84) Yang, Y.; Feng, Y.; Chen, Z.; Feng, Y.; Huang, Q.; Ma, C.; Xia, Q.; Liang, C.; Zhou, L.; Islam, M. S.; et al. Strain engineering by atomic lattice locking in P2-type layered oxide cathode for high-voltage sodium-ion batteries. *Nano Energy* **2020**, *76*, 105061.

(85) Takeda, N.; Hoshino, S.; Xie, L.; Chen, S.; Ikeuchi, I.; Natsui, R.; Nakura, K.; Yabuuchi, N. Reversible Li storage for nanosize cation/anion-disordered rocksalt-type oxyfluorides: $LiMoO_2 - x$ LiF $(0 \leq x \leq 2)$ binary system. *J. Power Sources* **2017**, *367*, 122−129.

(86) Hoshino, S.; Glushenkov, A. M.; Ichikawa, S.; Ozaki, T.; Inamasu, T.; Yabuuchi, N. Reversible Three-Electron Redox Reaction of Mo^{3+}/Mo^{6+} for Rechargeable Lithium Batteries. *ACS Energy Lett.* **2017**, *2* (2), 733−738.

(87) Patra, B.; Kumar, K.; Deb, D.; Ghosh, S.; Gautam, G. S.; Senguttuvan, P. Unveiling a high capacity multi-redox $(Nb^{5+}/Nb^{4+}/Nb^{3+})$ NASICON-$Nb_2(PO_4)_3$ anode for Li-and Na-ion batteries. *J. Mater. Chem. A* **2023**, *11*, 8173−8183.

(88) Jian, Z.; Zhao, L.; Pan, H.; Hu, Y.-S.; Li, H.; Chen, W.; Chen, L. Carbon coated $Na_3V_2(PO_4)_3$ as novel electrode material for sodium ion batteries. *Electrochem. Commun.* **2012**, *14*, 86−89.

(89) Panin, R. V.; Drozhzhin, O. A.; Fedotov, S. S.; Khasanova, N. R.; Antipov, E. V. NASICON-type $NaMo_2(PO_4)_3$: Electrochemical activity of the Mo+ 4 polyanion compound in Na-cell. *Electrochim. Acta* **2018**, *289*, 168−174.

(90) Kawai, K.; Zhao, W.; Nishimura, S.-I.; Yamada, A. High-voltage $Cr^{4+/Cr3+}$ redox couple in polyanion compounds. *ACS Appl. Energy Mater.* **2018**, *1*, 928−931.

(91) Long, O. Y.; Gautam, G. S.; Carter, E. A. Assessing cathode property prediction via exchange-correlation functionals with and without long-range dispersion corrections. *Phys. Chem. Chem. Phys.* **2021**, *23*, 24726−24737.

(92) Vyazovkin, S.; Wight, C. Kinetics in solids. *Annu. Rev. Phys. Chem.* **1997**, *48*, 125−149.

(93) Spotte-Smith, E. W. C.; Petrocelli, T. B.; Patel, H. D.; Blau, S. M.; Persson, K. A. Elementary decomposition mechanisms of lithium hexafluorophosphate in battery electrolytes and interphases. *ACS Energy Lett.* **2023**, *8*, 347−355.

(94) Li, B.; Kan, C.; Hang, P.; Fang, Y.; Zuo, L.; Song, L.; Zhang, Y.; Yang, D.; Yu, X. Understanding the Influence of Cation and Anion Migration on Mixed-Composition Perovskite Solar Cells via Transient Ion Drift. *Phys. Status Solidi RRL* **2021**, *15*, 2100225.

(95) Park, A. R.; Son, D.-Y.; Kim, J. S.; Lee, J. Y.; Park, N.-G.; Park, J.; Lee, J. K.; Yoo, P. J. Si/Ti2O3/reduced graphene oxide nanocomposite anodes for lithium-ion batteries with highly enhanced cyclic stability. *ACS Appl. Mater. Interfaces* **2015**, *7*, 18483−18490.

(96) Zhang, X.; Zhang, Z.; Yao, S.; Chen, A.; Zhao, X.; Zhou, Z. An effective method to screen sodium-based layered materials for sodium ion batteries. *Npj Comput. Mater.* **2018**, *4* (1), 13.

(97) Englich, U.; Massa, W.; Tressaud, A. Structure of trisodium hexafluoromanganate (III). *Acta Crystallographica. Section C, Cryst. Struct.Commun.* **1992**, *48*, 6−8.

(98) Vyazovkin, S. Kinetic effects of pressure on decomposition of solids. *Int. Rev. Phys. Chem.* **2020**, *39*, 35−66.

(99) Mesnier, A.; Manthiram, A. Synthesis of LiNiO2 at moderate oxygen pressure and long-term cyclability in lithium-ion full cells. *ACS Appl. Mater. Interfaces* **2020**, *12*, 52826−52835.

(100) Sharifi-Asl, S.; Lu, J.; Amine, K.; Shahbazian-Yassar, R. Oxygen release degradation in Li-ion battery cathode materials: mechanisms and mitigating approaches. *Adv. Energy Mater.* **2019**, *9*, 1900551.

(101) Ji, H.; Urban, A.; Kitchaev, D. A.; Kwon, D.-H.; Artrith, N.; Ophus, C.; Huang, W.; Cai, Z.; Shi, T.; Kim, J. C.; Kim, H.; et al. Hidden structural and chemical order controls lithium transport in cation-disordered oxides for rechargeable batteries. *Nat. Commun.* **2019**, *10*, 592.

(102) Ouyang, B.; Artrith, N.; Lun, Z.; Jadidi, Z.; Kitchaev, D. A.; Ji, H.; Urban, A.; Ceder, G. Effect of Fluorination on Lithium Transport and Short-Range Order in Disordered-Rocksalt-Type Lithium-Ion Battery Cathodes. *Adv. Energy Mater.* **2020**, *10*, 1903240.

(103) Wang, S.; Fu, J.; Liu, Y.; Saravanan, R. S.; Luo, J.; Deng, S.; Sham, T.-K.; Sun, X.; Mo, Y. Design principles for sodium superionic conductors. *Nat. Commun.* **2023**, *14*, 7615.

(104) Zhu, C.; Wu, C.; Chen, C.-C.; Kopold, P.; van Aken, P. A.; Maier, J.; Yu, Y. A high power−high energy $Na_3V_2(PO_4)_2F_3$ sodium cathode: investigation of transport parameters, rational design and realization. *Chem. Mater.* **2017**, *29*, 5207−5215.

(105) Broux, T.; Bamine, T.; Fauth, F.; Simonelli, L.; Olszewski, W.; Marini, C.; Ménétrier, M.; Carlier, D.; Masquelier, C.; Croguennec, L. Strong Impact of the Oxygen Content in $Na_3V_2(PO_2)_2F_{3\text{-}y}O_y$ $0 \leq y < 0.5$ on Its Structural and Electrochemical Properties. *Chem. Mater.* **2016**, *28*, 7683−7692.

(106) Kawai, K.; Asakura, D.; Nishimura, S.-I.; Yamada, A. 4.7 V Operation of the Cr^{4+}/Cr^{3+} redox couple in $Na_3Cr_2(PO_4)_2F_3$. *Chem. Mater.* **2021**, *33* (33), 1373−1379.